Rabi-induced localization and resonant delocalization of a binary condensate in a spin-asymmetric quasiperiodic potential

Swarup K. Sarkar,[1] Sh. Mardonov,[2,3] E. Ya. Sherman,[4,5,6] and Pankaj K. Mishra[1]
[1]*Department of Physics, Indian Institute of Technology Guwahati, Guwahati, Assam 781039, India*
[2]*New Uzbekistan University, Movarounnahr street 1, Tashkent 100000, Uzbekistan*
[3]*Ulugh Beg Astronomical Institute, Tashkent 100052, Uzbekistan*
[4]*Department of Physical Chemistry, University of the Basque Country UPV/EHU, 48940 Leioa, Spain*
[5]*IKERBASQUE, Basque Foundation for Science, Bilbao, Spain*
[6]*EHU Quantum Center, University of the Basque Country UPV/EHU, 48940 Leioa, Spain*

(Received 30 June 2025; accepted 8 September 2025; published 3 October 2025)

We theoretically investigate the ground state and dynamics of a Rabi-coupled pseudospin-1/2 Bose-Einstein condensate, where only one spin component is subjected to an external potential. We show that in the quasiperiodic potential the Rabi coupling induces localization between the components as it is raised above the threshold value. Interestingly, the localization is mutually induced by both components for the quasiperiodic confinement, whereas for a harmonic trap the localization is induced in the potential-free component by interaction with that confined in the potential. Further, we explore the condensate dynamics by implementing a periodic driving of the Rabi frequency, where various frequency-dependent delocalization patterns, such as double- (triple)-minima, treelike (parquetlike), and frozen distributions with a correlated propagation of different spin populations are observed in the condensate density. These features pave the way to control the condensate mass and spin density patterns, both in the stationary and dynamical realizations.

DOI: 10.1103/f67w-kd5j

I. INTRODUCTION

Bose-Einstein condensates (BECs), as macroscopic quantum states of matter, offer a highly controllable platform for exploring fundamental quantum phenomena, including the effects of disorder and interactions in low-dimensional systems. Among the most intriguing phenomena observed in such systems is the Anderson localization, originally proposed to describe the suppression of electronic diffusion in the disordered media [1], since then it has become a typical model for understanding the localization in a wide variety of complex systems. These include photonic lattices [2–6], microwaves [7–10], acoustic waves [11], and ultracold atomic gases [12,13]. In ultracold atomic gases, the weakly interacting BECs have been a suitable platform for exploring the localization of the quantum matter waves. Following the first experimental realization of localization of the condensate in the random [12] and quasiperiodic [13] potentials, the field has witnessed a great number of theoretical and experimental works. Various analytical [14,15] and numerical [16–20] approaches based on the mean-field Gross-Pitaevskii (GP) equation have been used to investigate the complex interplay between disorder and interactions on the localization.

Recently, the experimental realization of pseudospin-1/2 BECs where two hyperfine state are coupled with the synthetic spin-orbit (SO) and Rabi couplings generated using the Raman lasers [21] has become a fertile ground for investigating the rich physics of spin-dependent localization in condensates in quasiperiodic [22–24] and random potentials [25–27]. These systems also exhibit very intriguing nonlinear dynamics due to the spin-dependent velocities [28–30]. Additionally, it has been reported that the interplay between the inter- and intraspecies interactions, especially for a lifted Manakov's symmetry [31,32], where the nonlinear contribution to the BEC energy depends on the spin orientation, can produce a spatially asymmetric localization of the condensate [27].

A comprehensive understanding of localization in SO and Rabi coupled BECs remains challenging due to the complex interplay between disorder, interactions, and spin-related couplings [27], especially if SO and Rabi coupling do not commute. While the SO coupling promotes a spatial decoupling of spin components, the Rabi interaction fosters their coupling. To address this complexity, various simplified models have been proposed in recent years. Those often involve asymmetric spin-dependent potentials, where one spin component experiences a trapping potential while the other does not. In such setups, the trapped component exhibits localization, which in turn induces localization in the untrapped one either through density-density interaction or through the Rabi coupling. In this context, Wang *et al.* [33] investigated induced localization in an SO-coupled BEC confined in a double-well potential. They demonstrated that an imbalance between intra- and interspecies interactions can drive a transition from a spin-balanced phase to a spin-localized phase. Similarly, Santos and Cardoso [34] explored the localization in binary BEC where one component is trapped in a quasiperiodic potential

Published by the American Physical Society under the terms of the Creative Commons Attribution 4.0 International license. Further distribution of this work must maintain attribution to the author(s) and the published article's title, journal citation, and DOI.

and coupled to the free component via linear Rabi coupling and reported the related induced localization.

Experimentally, tuning SO coupling has posed a severe challenge to the researchers. Several studies have proposed controlling SO coupling through rapid modulation of laser intensities [35,36]. In a similar vein, time-modulated Rabi frequencies have been used to realize quantum phases [37], artificial gauge fields [38], matter-wave control [39], and to probe Landau-Zener tunneling [40,41]. For rapid modulation, Deconinck *et al.* [42] derived analytical solutions for linearly coupled Gross-Pitaevskii equations using a unitary transformation that absorbs the time-dependent Rabi frequency under Manakov's symmetry. Building on this, Nistazakis *et al.* [43] numerically implemented Rabi switch to transfer nonlinear structures between components, with reduced efficiency observed when the symmetry is broken. More recently, Abdullaev *et al.* [44] investigated parametric resonances and Josephson-like oscillations in SO-coupled BECs under time-modulated Raman coupling.

As we have seen, Rabi coupling significantly influences the ground state and dynamics of binary condensates. Trombettoni *et al.* [45] developed a theoretical framework showing that Rabi coupling enables population exchange in deep optical lattices. It also mediates the transformation of dark solitons into vector dark solitons [46], and affects miscibility in both nondipolar [47,48] and dipolar condensates [49,50], where it is crucial for immiscibility-miscibility transitions [49]. Moreover, it facilitates complex excitations such as vector rogue waves in multicomponent BECs [51], stabilizes solitonlike states under time-modulated coupling in quasi-two-dimensional (quasi-2D) systems [52], and inhibits vortex formation in rotating spinor BECs [53].

Although the model analysis of induced localization by Santos and Cardoso [34] provides a basic understanding of the roles played by Rabi coupling and interactions in the emergence of localized states, many fundamental aspects, both stationary and dynamical, of these states remain largely unexplored. In this work we study and understand these intriguing localizations and delocalizations demonstrating a rich set of quantum mechanical effects.

This paper is organized as follows. In Sec. II, we formulate the mean-field model with binary Gross-Pitaevskii equations and main observables to characterize the system of interest. Section III presents numerical results by showing the effect of linear Rabi coupling in the ground state, including the critical behavior of the localization and a strong impact of even weak nonlinearities. Subsequently, in Sec. IV we discuss the effect of time-periodic Rabi frequency on the localized condensates, both linear and those with lifted Manakov's symmetry of nonlinearities. Finally, we conclude our work in Sec. V and present some details, including a comparison of induced localization in quasiperiodic and harmonic traps, in the Appendix.

II. MEAN-FIELD MODEL AND OBSERVABLES

In this section we discuss the mean-field dynamical model used in the present work and define the relevant observables used to characterize the induced localizations.

A. Coupled Gross-Pitaevskii equations

We consider a pseudospin-1/2 quasi-one-dimensional condensate trapped strongly in the transverse direction, modeled by the coupled dimensionless Gross-Pitaevskii equations (experiment-related units will be presented below) [27,34,54]:

$$\mathrm{i}\frac{\partial\psi_\uparrow}{\partial t} = \left[-\frac{1}{2}\frac{\partial^2}{\partial x^2}+g_{\uparrow\uparrow}|\psi_\uparrow|^2+g_{\uparrow\downarrow}|\psi_\downarrow|^2+V_\uparrow(x)\right]\psi_\uparrow+\Omega_0\psi_\downarrow, \tag{1a}$$

$$\mathrm{i}\frac{\partial\psi_\downarrow}{\partial t} = \left[-\frac{1}{2}\frac{\partial^2}{\partial x^2}+g_{\downarrow\downarrow}|\psi_\downarrow|^2+g_{\downarrow\uparrow}|\psi_\uparrow|^2+V_\downarrow(x)\right]\psi_\downarrow+\Omega_0\psi_\uparrow, \tag{1b}$$

where $\psi_\uparrow$ and $\psi_\downarrow$ [$\psi_{\uparrow,\downarrow} \equiv \psi_{\uparrow,\downarrow}(x,t)$] represent the (pseudo) spin-up and (pseudo) spin-down components of the condensate wave function $\boldsymbol{\psi} = (\psi_\uparrow, \psi_\downarrow)^{\mathrm{T}}$, respectively, where T stands for transposition. For stationary states $\psi_{\uparrow,\downarrow}(x,t) = \psi_{\uparrow,\downarrow}(x)\exp(-\mathrm{i}\mu t)$, where μ is the chemical potential. Here, $g_{\uparrow\uparrow}$ and $g_{\downarrow\downarrow}$ are the intraspecies interaction strengths, $g_{\uparrow\downarrow}$, and $g_{\downarrow\uparrow}$ are interspecies interactions (with $g_{\uparrow\uparrow} = g_{\downarrow\downarrow} = g_{\uparrow\downarrow} = g_{\downarrow\uparrow}$ corresponding to the Manakov's symmetry [31]), and Ω_0 is the Rabi coupling strength. From now on for brevity, we will remove the (x,t) notations in $\psi_{\uparrow(\downarrow)}$ when it does not cause confusion.

The GPEs (1a) and (1b) correspond to the binary BEC Hamiltonian with the linear Rabi coupling $\Omega_0\sigma_x$ with σ_x being the corresponding Pauli matrix. The trapping potential is $V_j(x)$ with $j = \{\uparrow, \downarrow\}$. Here we consider the condensate interacting with the trapping potential only in the spin-up component [34], such as:

$$V_\uparrow(x) = V(x), \quad V_\downarrow(x) = 0. \tag{2}$$

In general, this spin asymmetry makes the BEC localization features qualitatively different from those expected for the $V_\downarrow(x) = V_\uparrow(x) = V(x)$ potential. In order to analyze the localization induced by one spin component on the other we consider $V(x)$ as a quasiperiodic potential of the form:

$$V(x) = V_1\sin^2(k_1x) + V_2\sin^2(k_2x), \tag{3}$$

where V_1 and V_2 are the primary and secondary optical lattice amplitudes, respectively. This potential has minima at points $x = x_i \geqslant 0$ and $x = -x_i < 0$ ($i = 0, 1\ldots, x_0 = 0$, and $x_{i+1} > x_i$) where

$$V'(x) = V_1k_1\sin(2k_1x_i) + V_2k_2\sin(2k_2x_i) = 0, \tag{4}$$

$$V''(x) = 2\left(V_1k_1^2\cos(2k_1x_i) + V_2k_2^2\cos(2k_2x_i)\right) > 0,$$

characterized by corresponding local oscillator frequencies $\omega_i = \sqrt{V''(x)}$ at $x = x_i$.

In experiments, the pseudospin-1/2 Rabi-coupled BEC can be realized by using two hyperfine states of ^{87}Rb atoms as pseudospin-up $|\uparrow\rangle \equiv |F = 1, m_F = 0\rangle$ and spin-down $|\downarrow\rangle \equiv |F = 1, m_F = -1\rangle$, which are coupled by a pair of Raman lasers with wavelength 804.1 nm. Recoil wave vector $k_L = \sin(\theta/2)k_p$, where k_p is the photon wave vector, and the recoil energy $E_L = \hbar^2k_L^2/2m$ (with m being the atomic mass) provide relevant scales for tuning the SO and Rabi couplings [21,36]. In quasi-one-dimension, the condensate is strongly confined in transverse direction with $\omega_\perp \sim 10^3\,\mathrm{s}^{-1}$ with corresponding $a_\perp \sim 1$ μm and $\hbar\omega_\perp \sim 5$ nK. The inter and intraspin scatter-

ing lengths being typically of the order of 5 nm can be further controlled by using Feshbach resonances.

To obtain the dimensionless Eqs. (1a) and (1b), we consider the transverse harmonic oscillator length $a_\perp = \sqrt{\hbar/(m\omega_\perp)}$ as a characteristic length scale with $\omega_\perp$ as the transverse harmonic trapping frequency, $\omega_\perp^{-1}$ as the time scale and $\hbar\omega_\perp$ as the characteristic energy scale. The interaction parameters can be defined in terms of $g_{\uparrow\uparrow,(\downarrow\downarrow)} = 2\mathcal{N}a_{\uparrow\uparrow,(\downarrow\downarrow)}/a_\perp$, and $g_{\uparrow\downarrow} = 2\mathcal{N}a_{\uparrow\downarrow}/a_\perp$, where, $a_{\uparrow\uparrow,(\downarrow\downarrow)}$ and $a_{\uparrow\downarrow}$ represent the intra- and intercomponent scattering lengths, respectively, and $\mathcal{N}$ represents the total number of atoms in the condensate. The dimensionless Rabi coupling Ω_0 is defined in the units of $2\omega_\perp$ with the wave function being rescaled with $\sqrt{a_\perp}$.

B. Definition of spin-dependent observables

To characterize the localization and delocalization at different spatial scales we start with the occupation numbers N_j, where

$$N_j = \int_{-\infty}^{\infty} |\psi_j|^2 dx, \tag{5}$$

with $N_\uparrow + N_\downarrow = 1$. The width w_j is given by

$$w_j^2 = \frac{1}{N_j}\int_{-\infty}^{\infty} (x - \langle x_j\rangle)^2 |\psi_j|^2 dx, \tag{6}$$

where the center-of-mass position $\langle x_j\rangle$:

$$\langle x_j\rangle = \frac{1}{N_j}\int_{-\infty}^{\infty} x|\psi_j|^2 dx. \tag{7}$$

The shape is characterized by the inverse participation ratio (IPR) χ_j:

$$\chi_j = \frac{1}{N_j^2}\int_{-\infty}^{\infty} |\psi_j|^4 dx. \tag{8}$$

We also utilize the spin miscibility parameter characterizing the joint distribution of densities of spin components defined as

$$\eta = 2\int_{-\infty}^{\infty} |\psi_\uparrow||\psi_\downarrow| dx, \tag{9}$$

with $\eta = 1$ ($\eta = 0$) corresponding to fully miscible (immiscible) realizations. For real wave functions $\eta = |\langle\sigma_x\rangle|$.

After obtaining the initial ground state $\psi_j(x, 0)$, we use the time-varying Rabi frequency to study the dynamics of the condensate. For this purpose we calculate the time-correlation function corresponding to different states, which is defined in terms of the absolute value of the overlap function as,

$$C_j(t) = \left|\int_{-\infty}^{\infty} \psi_j(x, t)\psi_j(x, 0)dx\right|, \tag{10}$$

where $C_j(0) = N_j(0)$. As we will see below, the criteria of induced delocalization can be obtained by considering evolution of $C_j(t)$ for given spin state [55].

III. GROUND STATE OF INDUCED LOCALIZATION

To understand the role of Rabi coupling in inducing localization and shaping the ground-state structure of a binary condensate, we present a detailed analysis of the ground-state profiles of the spin components when they are linearly coupled via the Rabi frequency. We begin by examining the noninteracting case and investigate how Rabi coupling influences localization in the spin-down component induced by the spin-up component, and vice versa. The results of imaginary time propagation are complemented by an eigenmode analysis, which allows us to determine the threshold Rabi frequency beyond which induced localization emerges in the spin components. We then extend this analysis to include interactions, exploring how Rabi coupling affects induced localization in the interacting binary condensate.

A. Calculation procedure

We begin our analysis by presenting the numerical results obtained by solving the pair of coupled GPEs [Eqs. (1a) and (1b)] in which the spin-up component is trapped with a bichromatic lattice potential (3) and the trapless spin-down component interacts with spin-up component by linear Rabi coupling. For all of our calculations, the primary and secondary lattice strengths are considered as $V_1 = 1$ and $V_2 = 0.5$, respectively, with wave numbers $k_1 = 0.35$ and $k_2/k_1 = (\sqrt{5} - 1)/2$, corresponding to the inverse golden ratio.

To obtain the ground state we begin with the imaginary time propagation (ITP) considering the coupled GPEs (1) with the potential (3) using time-splitting Fourier spectral method [56]. However, since the spin-down component is not subjected to the external potential, obtaining the ground state using the ITP becomes particularly challenging for low Rabi coupling strengths ($\Omega_0 < 0.2$). To address this, we also solve the linearized GPEs as an eigenvalue problem to compute the full spectrum of eigenvalues and corresponding eigenstates without any self-interactions.

This matrix method involves constructing a $(2N \times 2N)$ matrix that represents the coupled linear GPEs, where N is the number of grid points for the spatial domain being discretized at $x = [-L, L]$ with $L = N\Delta x/2$. We use the same spatial step size $\Delta x = 0.025$ and grid size $N = 8192$ as in the ITP to ensure consistency. Once the matrix is constructed, it is diagonalized using the arpack package in python. A key advantage of this matrix-based method is that it treats the problem as stationary, making it well suited for exploring regimes with weak Rabi coupling. This allows us to probe the low Ω_0 region more effectively than with the ITP approach.

Thus, to obtain the ground state for noninteracting part of the problem we use both the ITP and matrix method to solve the coupled GPEs, while, at nonzero self-interaction, we resort to the ITP only, by choosing the initial state as an antisymmetric Gaussian wave function: $\psi_\uparrow(x) = -\psi_\downarrow(x)$. The imaginary and real-time propagation is utilized with time step $\Delta t = 10^{-4}$ to study the ground state and dynamics of the condensate.

B. Ground state of noninteracting BEC: Rabi-induced localization

As the spin-up component interacts with the quasiperiodic potential, the other one is expected to be correlated with it due to the Rabi coupling acting since minimization of the Rabi energy requires similarity of these densities (see Appendix A for

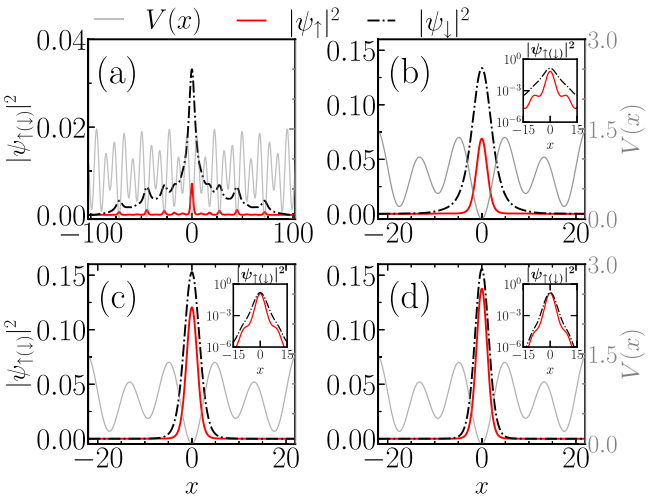


FIG. 1. The BEC density $|\psi_{\uparrow(\downarrow)}|^2$ for different values of Rabi coupling Ω_0: (a) $\Omega_0 = 0.08$, (b) $\Omega_0 = 0.2$, (c) $\Omega_0 = 0.4$, and (d) $\Omega_0 = 0.6$. Increasing Ω_0 equalizes the spin-up and spin-down profiles. In the insets of (b)–(d), the density is plotted on a semilogarithmic scale to highlight the exponential and Gaussian behavior of the localized condensate, as it depends on Ω_0. Here, all the interactions $g_{\uparrow\uparrow} = g_{\downarrow\downarrow} = 0$.

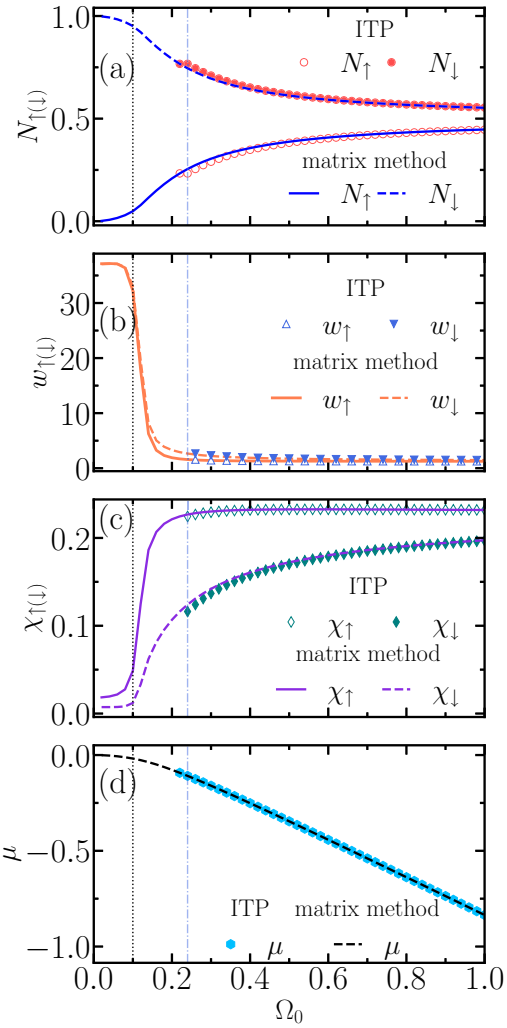


FIG. 2. (a) Variation of population $N_{\uparrow(\downarrow)}$, (b) width $w_{\uparrow(\downarrow)}$, (c) IPR $\chi_{\uparrow(\downarrow)}$, and (d) chemical potential μ as a function of Ω_0 at $V_2/V_1 = 0.5$, $V_1 = 1.0$, $g = 0$. Here, the solid and dashed lines represent the entities obtained with the matrix method. The quantities obtained by the ITP method are shown by markers. Increase in Ω_0 results in transfer of probability from $\downarrow$ to $\uparrow$ component. The increasing IPR indicates that the spin-down and spin-up components are tending to localize with the same profile due to the Rabi coupling, while spin-up is originally localized by the $V_\uparrow(x)$ potential.

details). To quantitatively investigate the localization induced by the Rabi coupling, in Fig. 1, we present the condensate density profile $|\psi_{\uparrow(\downarrow)}|^2$ for different values of Ω_0. At very small $\Omega_0 = 0.08$, both components are broadly distributed over the $[-L, L]$ range, showing different patterns. While $|\psi_\uparrow|^2$ is located mainly in the vicinities of the minima x_i [see Eq. (4)], $|\psi_\downarrow|^2$ shows a more continuous distribution with peaks near x_i minima [see Fig. 1(a)]. The distinct peaks of $|\psi_\downarrow(x_i)|^2$ demonstrate the effect of Rabi-coupling to couple the components even at very low values of Ω_0. Conversely, for larger values of Ω_0, both components are localized near the minima at $x = 0$ [see Figs. 1(b) and 1(c)]. With the further increase of Ω_0, $|\psi_\downarrow|^2$ closely follows the $|\psi_\uparrow|^2$. In this context, it is instructive to compare the insets in Figs. 1(b)–1(d). The inset in Fig. 1(c) depicts that for a moderate Rabi coupling, the BEC shows two distinct types of localization: the exponential one for the spin-down and the Gaussian one for the spin-up states, respectively. For a strong Rabi coupling, where $\Omega_0 \sim \lambda$, both components show the Gaussian-like localization. This is in agreement with the findings of Santos and Cardoso in Ref. [34].

The effect of the Rabi coupling can be further understood by analyzing the population N_j [Fig. 2(a)], width w_j [Fig. 2(b)], and IPR χ_j [Fig. 2(c)], and chemical potential μ [Fig. 2(d)] of the condensate. This behavior can be compared with induced localization for the harmonic trap with the frequency ω_0 [see Eq. (4) and Appendix A].

The obtained population imbalance forms the BEC spin polarization. In spin-orbit coupled multicomponent condensates such modifications typically arise from unequal interactions lifting Manakov's symmetry of the spin states [27]. In the present case, the spin-asymmetric potential similarly induces population imbalance, so tuning the Rabi coupling offers an additional means of controlling spin states in BECs, beyond the conventional approach of tuning atomic interactions. An example of this effect is provided in Appendix C.

Figure 2(a) shows that for weak Rabi coupling $\Omega_0 \lesssim 0.2$ the trapped condensate population $N_\uparrow \ll 1$, while $N_\downarrow$ is close to 1 because at small Ω_0 one has $|\psi_\uparrow|^2 \ll |\psi_\downarrow|^2$, corresponding to the fact that minimizing the BEC energy requires a large occupation of the broad spin $\downarrow$ state. Increasing the Rabi coupling tends to equalize the population of both components. On the other hand, condensate width is very large for $\Omega_0 < 0.1$, beyond that the decreasing width $w_{\uparrow(\downarrow)}$ reveals that the increase in Ω_0 leads to mutual localization of the spin-related components eventually following each other [see Fig. 2(b)]. Interestingly, for the harmonic potential (see Appendix), this localization process is different because of the

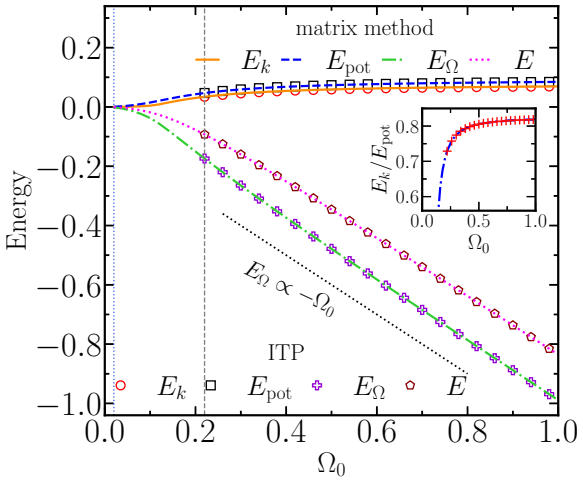


FIG. 3. Variation of different energies defined by Eqs. (11)–(13) as a function of Rabi coupling Ω_0 at $V_2/V_1 = 0.5, V_1 = 1.0$. As Ω_0 increases, the ratio of potential $E_{\rm pot}$ and kinetic E_k energies approximately saturates toward ∼0.85, as shown in the inset, while the dominating negative E_Ω minimizes the total energy $E = E_{\rm pot} + E_k + E_\Omega$. The black dotted line is presented to highlight the behavior of $E_\Omega \propto -\Omega_0$.

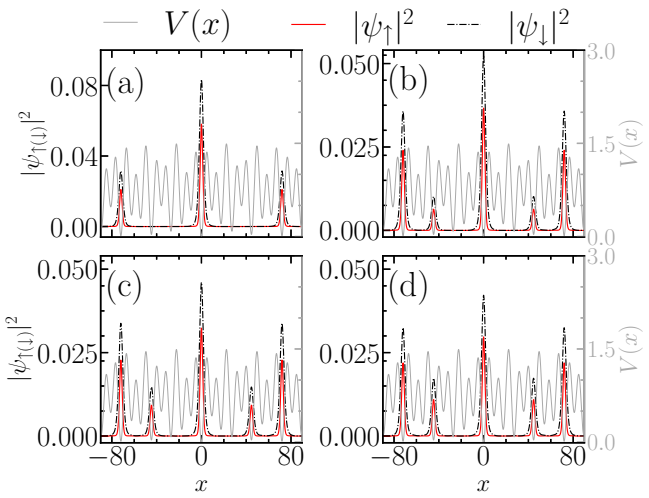


FIG. 4. The condensate density $|\psi_{\uparrow(\downarrow)}|^2$ for different self-interaction strengths: (a) $g = 0.1$, (b) $g = 0.3$, (c) $g = 0.4$, and (d) $g = 0.5$. Increasing the repulsive interaction causes the condensate to break into multiple fragments, forming several peaks at potential minima located at $x \neq 0$. The other parameters are kept as follows: $V_1 = 1.0, V_2 = 0.5, k_1 = 0.35, k_2/k_1 = (\sqrt{5}-1)/2$, and $\Omega_0 = 0.3$.

strong confinement of the spin-up component in the harmonic trap. Comparing width $w_{\uparrow(\downarrow)}$ and IPR $\chi_{\uparrow(\downarrow)}$ in Figs. 2(b) and 2(c) clearly shows that $\chi_\downarrow$ increases with Ω_0, demonstrating again the Rabi-induced localization, complemented by inset semilogscale profiles in Fig. 1. In that context, the linearly decreasing chemical potential $\mu \approx -\Omega_0$ [Fig. 2(d)] at $\Omega_0 \geqslant 0.5$ defines the formation of bound state of similar spin-up and spin-down components due to a strong coupling.

In Fig. 3 we show different energies as a function of Ω_0 with the other parameters the same as in Fig. 2. These energies are defined as follows. The potential energy corresponding to Eq. (2):

$$E_{\rm pot} = \int_{-\infty}^{\infty} V_\uparrow(x)|\psi_\uparrow|^2 dx, \tag{11}$$

the kinetic energy

$$E_k = \frac{1}{2}\int_{-\infty}^{\infty} |\psi_\uparrow'|^2 dx + \frac{1}{2}\int_{-\infty}^{\infty} |\psi_\downarrow'|^2 dx, \tag{12}$$

and the Rabi coupling energy

$$E_\Omega = \Omega_0 \int_{-\infty}^{\infty} (\psi_\downarrow^* \psi_\uparrow + \psi_\uparrow^* \psi_\downarrow) dx. \tag{13}$$

For small Ω_0, the potential and kinetic energies increase and then approximately saturate. Throughout the variation these energies are relatively close to each other. As Ω_0 increases, the ratio of $E_k/E_{\rm pot}$ saturates toward 0.85 as shown in the inset of Fig. 3, while the Rabi-coupling contribution E_Ω, decreasing approximately as $-\Omega_0$, dominates in the total energy. The strong Rabi coupling requires $\psi_\uparrow \approx -\psi_\downarrow$ implying that in this limit localization in potential in Eq. (2) is similar to localization in spin-independent potential $V_\uparrow(x) = V_\downarrow(x) = V(x)$ (see Appendix A for details).

C. Ground state of self-interacting condensate

In this section we explore the effect of the self-interaction with lifted Manakov's symmetry described by a single parameter g, where $g = g_{\uparrow\uparrow} = g_{\downarrow\downarrow}$ and $g_{\uparrow\downarrow} = g_{\downarrow\uparrow} = 0$, without nonlinear coupling between different spin components, on the ground state of the condensate. The resulting self-interaction energy is given by:

$$E_{\rm int} = \frac{g}{2}\sum_{j=\uparrow,\downarrow}\int_{-\infty}^{\infty} |\psi_j|^4 dx = \frac{g}{2}\sum_{j=\uparrow,\downarrow} N_j^2 \chi_j. \tag{14}$$

In Fig. 4, we show the condensate density for different g by keeping Rabi coupling at $\Omega_0 = 0.3$. At $g = 0$, the condensate is perfectly localized near $x = 0$ as seen in Fig. 1(b). The repulsive intraspecies interactions result in expanding the condensate from the central minimum and leads to its fragmentation at various positions. For example, in Fig. 4(a) $g = 0.1$, the BEC localized at $x = 0$ fragments with two additional peaks at $x \sim \pm 80$, where another minimum of $V(x)$ is located. With the further increase in g, the condensate breaks into more fragments as in Figs. 4(c) and 4(d) fragmentation occurs with five peaks situated around $x \sim \pm 70, \pm 80$, and $x = 0$.

This strong effect of self-interaction is the specific feature of the quasiperiodic potential having a variety of minima with small $V(x_i)$ and close ω_i. Thus, a relatively weak self-repulsion can effectively redistribute the condensate density between these minima with similar energies. This effect of self-repulsion is enhanced by the fact that spread of spin-down component is not influenced by the quasiperiodic potential. At a moderate or strong Ω_0, where $|\psi_\downarrow| \approx |\psi_\uparrow|$, the critical self-interaction $g_{\rm cr}$ that begins the occupation of the wing $x_i \neq 0$ minima, can be estimated as $g_{\rm cr}\chi_0/2 \approx E_i - E_0$, where $\chi_0 = \sqrt{\omega_0/2\pi}$ is the IPR of the state localized near $x = 0$ and E_i

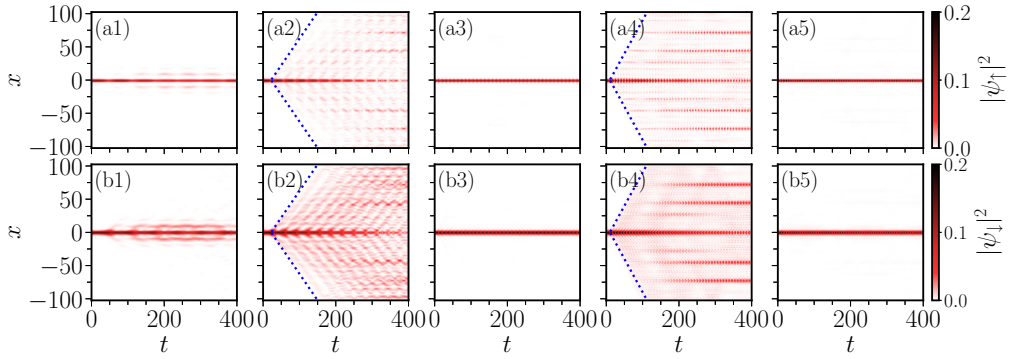


FIG. 5. Pseudo-color-map representation of the condensate densities $|\psi_\uparrow|^2$ (top) and $|\psi_\downarrow|^2$ (bottom) in the (t, x) plane for different frequencies $\omega_{\rm osc}$: (a1), (b1) $\omega_{\rm osc} = 0.1$, (a2), (b2) $\omega_{\rm osc} = 0.2$, (a3), (b3) $\omega_{\rm osc} = 0.4$, (a4), (b4) $\omega_{\rm osc} = 0.8$, and (a5), (b5) $\omega_{\rm osc} = 1.0$. For $\omega_{\rm osc} = 0.2$ (a2), (b2) and $\omega_{\rm osc} = 0.8$ (a4), (b4), the density expands. However, the expansion dynamics for $\omega_{\rm osc} = 0.8$ differ from those at $\omega_{\rm osc} = 0.2$. Specifically, at $\omega_{\rm osc} = 0.8$, the density $|\psi_{\uparrow(\downarrow)}|^2$ eventually settles at different potential minima (a4), (b4), whereas for $\omega_{\rm osc} = 0.2$ (a2), (b2), it expands by emitting jets with a nearly uniform velocity. For other $\omega_{\rm osc}$, the condensate remained localized around $x = 0$. The other parameters are $\Omega_0 = 0.4$, $\Omega_1 = 0.2$, and $g = 0$. (a1) and (b1) correspond to double- (triple)-minima evolution, panels (a2), (b2) and (a4), (b4) show treelike patterns while (a3), (b3) and (a5), (b5) correspond to a frozen behavior.

is the closest to $E_0 \approx \omega_0$ energy. Thus, even a relatively small $g \sim 0.1$ can cause density redistribution between the distant minima seen as the BEC fragmentation while the effect on g on the states near the $x = 0$ minimum becomes considerable at $g \sim \sqrt{2\pi\omega_0} \gtrsim 1$.

After analyzing the role of Rabi coupling in the induced localization of the noninteracting and interacting binary condensate now we proceed to explore the dynamics of the localized states.

IV. DYNAMICS OF INDUCED LOCALIZED CONDENSATES

In this section, we proceed to study the BEC dynamics caused by periodical driving with the time-modulated Rabi frequency as:

$$\Omega(t) = \begin{cases} \Omega_0, & t < 0 \\ \Omega_0 + \Omega_1 \sin(\omega_{\rm osc} t), & t > 0 \end{cases} \tag{15}$$

,where at $t < 0$ the condensate is in the ground state. For capturing the dynamics we use different entities such as the density, miscibility (9), and correlation function (10). To make the time modulation a (possibly strong) perturbation, we always maintain $\Omega_1/\Omega_0 = 1/2$ ratio and the oscillation frequency $\omega_{\rm osc}$ is varied within the interval from 0.1–1.0.

A. Effect of the oscillating Rabi frequency on the linear condensate

To begin our analysis for the linear condensate, in Fig. 5, we show the evolution of the density $|\psi_{\uparrow(\downarrow)}|^2$ in the (t, x) plane for oscillation frequencies ranging between $\omega_{\rm osc} = [0.1–1.0]$ while keeping $\Omega_0 = 0.4$, and $\Omega_1 = 0.2$ such that $\Omega(t)$ oscillates between a relatively weak (0.2) and a relatively strong (0.6) values (cf. Fig. 1). For $\omega_{\rm osc} = 0.1$ in Figs. 5(a1) and 5(b1), the density mainly remains localized near $x = 0$, although, due to the potential-free spin-down component, it exhibits oscillations within two nearest minima $\pm x_1$. This behavior demonstrates that the BEC acquires a relatively small energy, leading to confined oscillations within a double (triple) well.

Next, the density propagation at $\omega_{\rm osc} = 0.2$ [in Figs. 5(a2) and 5(b2)] exhibits driven expansion all over the space, indicating delocalization of the condensate. However, the effect is more pronounced for $|\psi_\downarrow|^2$ [(in Fig. 5(b2)] than for $|\psi_\uparrow|^2$ [in Fig. 5(a2)] due to the confinement of the latter. The spin-down component is emitted from the central minimum as separate jets with the velocity of the order of $\sqrt{\omega_0}$, corresponding to the spread a Gaussian wave packet with the initial energy $\sim\omega_0$ [see Eq. (4)]. The decreasing of $|\psi_\downarrow|^2$ in the vicinity of the $x = 0$ minimum pulls the $|\psi_\uparrow|^2$ out of this region and leads to its time dependence and delocalization. Simultaneously, increasing in $\Omega(t)$ to $\approx \Omega_0 + \Omega_1$ periodically pumps the probability from $\uparrow$ to $\downarrow$ component while lowering $\Omega(t)$ to $\approx \Omega_0 - \Omega_1$ during the same period causes emission of spin-down jets and, correspondingly, a decrease in the probability for the $\downarrow$component to be occupied. With the gradual reduction in the densities of both components near $x = 0$ point, accompanied by a decrease in their Rabi coupling, the efficiency of this process decreases.

Similarly, for $\omega_{\rm osc} = 0.8$ [see Figs. 5(a4) and 5(b4)], the condensate initially expands up to $t \lesssim 200$ and starts breaking symmetrically into multiple fragments at different $x \neq 0$ minima of $V(x)$. This feature is more clearly visible with different time snapshots of total density $|\psi|^2$ shown in Fig. 6. Comparison of Figs. 6(a) and 6(b) illustrates that at $\omega_{\rm osc} = 0.8$ [in Fig. 6(b)] the density symmetrically breaks into multiple fragments beyond $t > 200$ at $V(x)$ minima around $x \sim \pm 50, \pm 80$ and remains frozen there. In contrast, the density at $\omega_{\rm osc} = 0.2$ [in Fig. 6(a)] expands with uniform velocity being distributed uniformly all over the space, which we define as treelike expansion resulting in delocalization. A possible explanation for the two distinct types of delocalization phenomena is as follows: for lower oscillation frequencies such as $\omega_{\rm osc} = 0.2$, the timescale over which the condensate density expands is comparable to the semiadiabatic time scale associated with the modulation frequency of $\Omega(t)$. This leads to a relatively modest expansion of the condensate. In contrast, at $\omega_{\rm osc} = 0.8$,

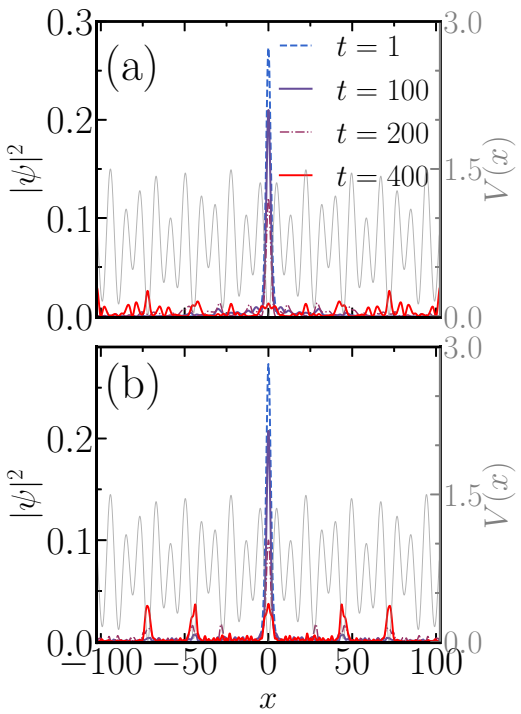


FIG. 6. The total density profile $|\psi|^2 = |\psi_\uparrow|^2 + |\psi_\downarrow|^2$ is shown at different time snapshots $t = (1, 100, 200, 400)$ for (a) $\omega_{\rm osc} = 0.2$ and (b) $\omega_{\rm osc} = 0.8$. For $\omega_{\rm osc} = 0.8$, the density fragments into four distinct minima of the potential located at nonzero positions $x \neq 0$ at large time snap ($t = 400$), whereas for $\omega_{\rm osc} = 0.2$, the condensate expands.

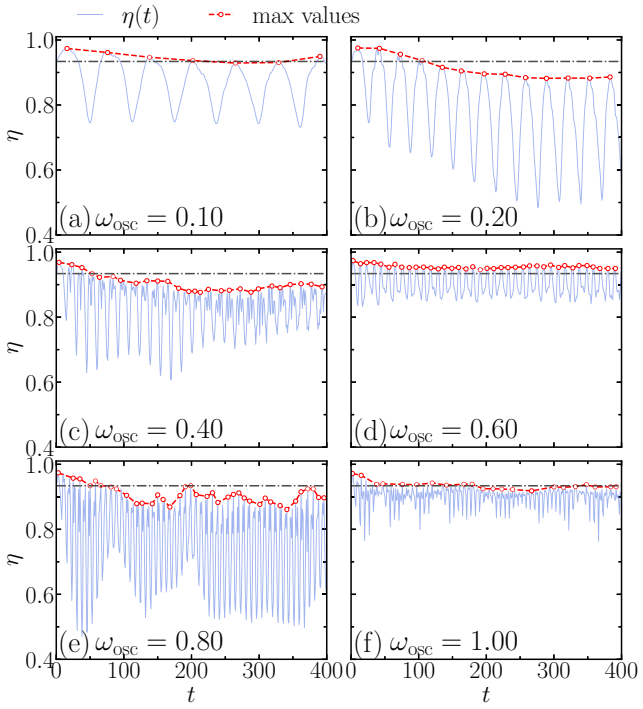


FIG. 7. Time dependence of miscibility η for different oscillation frequencies of the Rabi field $\omega_{\rm osc}$: (a) $\omega_{\rm osc} = 0.1$, (b) $\omega_{\rm osc} = 0.2$, (c) $\omega_{\rm osc} = 0.4$, (d) $\omega_{\rm osc} = 0.6$, (e) $\omega_{\rm osc} = 0.8$, and (f) $\omega_{\rm osc} = 1.0$. The black dash-dotted line indicates the initial miscibility $\eta(0) = 0.934$. The function $\eta(t)$ represents the miscibility after turning on the Rabi field ($\Omega_1 \neq 0$). A red circle-marked dashed line highlights the maximum values of $\eta(t)$. Comparing $\eta(0)$ with the red circled maxima shows that the miscibility gradually decreases over time for $\omega_{\rm osc} = 0.2$, 0.6, and 0.8, indicating expansion of the condensate.

the rapid variation of $\Omega(t)$ causes the condensate expansion time scale to become shorter relative to the modulation time scale of $\Omega(t)$, resulting in the condensate becoming effectively frozen at different minima. However, for other frequencies such as $\omega_{\rm osc} = 0.4$ [Figs. 5(a3) and 5(b3)] and 1.0 [Figs. 5(a5) and 5(b5)], the condensate remains localized near $x = 0$. At this juncture, it is worth noting that Nakamura *et al.* [57] theoretically reported the resonant driven levitation of binary condensates subjected to two distinct harmonic traps, similarly to the Franck-Condon effect in molecular physics.

Characterizing the localization and delocalization is a challenging task because of one of the components is potential free and Rabi coupling $\Omega_0 = 0.4$ is not strong enough. Therefore, the evolution of the density pattern cannot give much insight. In that context, we use other set of observables: miscibility $\eta(t)$ [Eq. (9)] and correlation functions $C_j(t)$ [Eq. (10)] to characterize these processes [55,58,59].

Given the unequal populations of the spin components, we analyze miscibility $\eta(t)$ to characterize differences in driven localization or delocalization. Figure 7 represents the miscibility $\eta(t)$ for the same oscillation frequencies as in Fig. 5. The maximum of $\eta(t)$ is highlighted with a red circle-marked dashed line in each panel from Figs. 7(a)–7(f), and the black dash-dotted line is drawn at $\eta(0) = 0.934$ to indicate the extent of miscibility. In addition it should be noted that the expansion of the condensate gets manifested in the decreasing trend of $\eta(t)$ from $\eta(0)$, as depicted by the red markers in Figs. 7(b), 7(c), and 7(e) for $\omega_{\rm osc} = 0.2$, 0.4, and 0.8, respectively. For other cases, the miscibility remains nearly constant. Therefore, the transition from localization to delocalization can be characterized through the decreasing miscibility $\eta(t) < \eta(0)$.

Furthermore, we compute the spin-projected correlation functions $C_j(t)$ (see Fig. 8) for the same set of $\omega_{\rm osc}$ as in Fig. 7. Notably, $C_\uparrow(t)$ (purple solid line) and $C_\downarrow(t)$ (orange dash-dotted line) consistently maintain a close to π phase difference for all the cases due to periodic probability pumping from spin-$\uparrow$ to spin-$\downarrow$ component. For comparison, we also include the stationary correlation functions, represented by a sky blue dashed line for $C_\uparrow(0)$ and a green dotted line for $C_\downarrow(0)$. The decrease in $C_j(t)$ with time demonstrates the condensate escape from the ground state. Note that $C_j(t)$ are close to $C_j(0)$ for $\omega_{\rm osc} = 0.1$, 0.6, 1.0 as shown in Figs. 8(a), 8(d), and 8(f), respectively. Thus, with the course of time, the spin components remain close to the initial state in the vicinity of $x = 0$, as mentioned earlier in Fig. 5. Conversely, for $\omega_{\rm osc} = 0.2$ [in Fig. 8(b)] and $\omega_{\rm osc} = 0.8$ [in Fig. 8(e)], the $C_j(t)$ decrease by following power laws with approximate exponents $t^{-0.5}$ and $t^{-0.3}$, respectively. Also, at $\omega_{\rm osc} = 0.4$ [in Fig. 8(c)], the $C_j(t)$ show a feeble decrement with time. Thus, the escape of the condensate can be characterized through the powerlike decrease of the time-correlation functions. Also note that the relative decrease in $C_\uparrow(t)$ compared to $C_\uparrow(0)$ is less than that of $C_\downarrow(t)$, because the trapping potential in spin-up component tries to prevent its decrease.

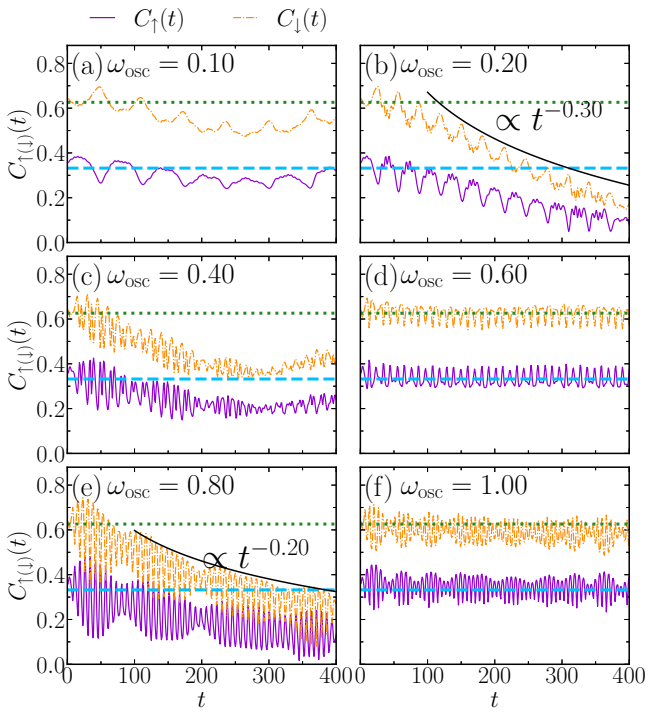


FIG. 8. Temporal variation of the correlation function $C_{\uparrow(\downarrow)}(t)$ is shown for different oscillation frequencies ω_{osc}: (a) $\omega_{osc} = 0.1$, (b) $\omega_{osc} = 0.2$, (c) $\omega_{osc} = 0.4$, (d) $\omega_{osc} = 0.6$, (e) $\omega_{osc} = 0.8$, and (f) $\omega_{osc} = 1.0$. The spatiotemporal expansion of the condensate can be characterized by a power-law behavior of the form $t^{-\alpha}$ for $\omega_{osc} = 0.2$ and $\omega_{osc} = 0.8$, where $C_{\uparrow(\downarrow)}(t)$ exhibits a decreasing trend over time. The values of the exponent α are found to be 0.3 for $\omega_{osc} = 0.2$, and 0.2 for $\omega_{osc} = 0.8$. The dashed line (sky blue color), and dotted line (green color) is drawn to compare with the static case $\Omega_1 = 0$. The other parameters are same as Fig. 5.

So far, our analysis reveals several effects of periodic Rabi frequency towards delocalization of the condensate in the absence self-interactions. Following this, in the next section we explore the effect of $\Omega(t)$ at self-repulsion $g > 0$.

B. Dynamics of induced delocalization in the presence of interaction ($g > 0$)

As we have discussed earlier in Sec. III C, the self-repulsions lead to fragmentation of the condensate across different potential minima and the number of fragments increases with the strength of the self-interaction. Our aim here is to analyze the dynamics of those fragmented condensates under the influence of the periodic Rabi frequency.

To begin with, in Fig. 9 we present the evolution of the densities $|\psi_{\uparrow(\downarrow)}|^2$ for different ω_{osc}, while keeping $g = 0.3$, $\Omega_0 = 0.3$, and $\Omega_1 = 0.15$. Initially at $t = 0$, five distinct fragments are located around $x = 0, \pm 25, \pm 75$ [see Fig. 4(b)]. At $\omega_{osc} = 0.15$ [Figs. 9(a1) and 9(b1)], the condensate expands by jet emission from each of these fragments. At $\omega_{osc} = 0.3$ [Figs. 9(a2) and 9(b2)], the expansion becomes less pronounced compared to the previous case. In contrast, for $\omega_{osc} = 0.6$, the fragmented densities remain localized at their respective positions, exhibiting no significant expansion over time. However, for higher frequencies such as $\omega_{osc} = 0.75$ and 0.9, the condensate symmetrically breaks into more fragments as time progresses. Since interactions inherently induce the BEC fragmentation, the exact identification of dynamically localized and delocalized behavior becomes even more challenging than in the noninteracting case.

To quantify different regimes, in Fig. 10 we show the miscibility $\eta(t)$ for different ω_{osc}. Unlike the noninteracting case, here the decrease in $\eta(t)$ from $\eta(0)$ does not provide significant information into the condensate expansion. Nevertheless, the amplitude of $\eta(t)$ provides a qualitative explanation of the phenomena. For instance, in Fig. 10(a), the amplitude of $\eta(t)$ lies in the range $0.5 \lesssim \eta(t) \lesssim 0.9$. Similarly, for $\omega_{osc} = 0.3$ and 0.6 [Figs. 10(b) and 10(d)], $\eta(t)$ oscillates between $0.6 \lesssim \eta(t) \lesssim 0.9$ and $0.4 \lesssim \eta \lesssim 0.9$, respectively. On the other hand, for higher frequencies, $\eta(t)$ remain within a narrow interval, i.e., $0.7 \lesssim \eta \lesssim 0.9$. However, the large amplitude variation of $\eta(t)$ demonstrates the expansion from the condensate's initial positions, whereas, the small amplitude variation signifies no as such expansion of the condensate from their respective positions.

Furthermore, we examine the correlation function $C_j(t)$ in Fig. 11 for the same set of ω_{osc} as shown in Fig. 10. The

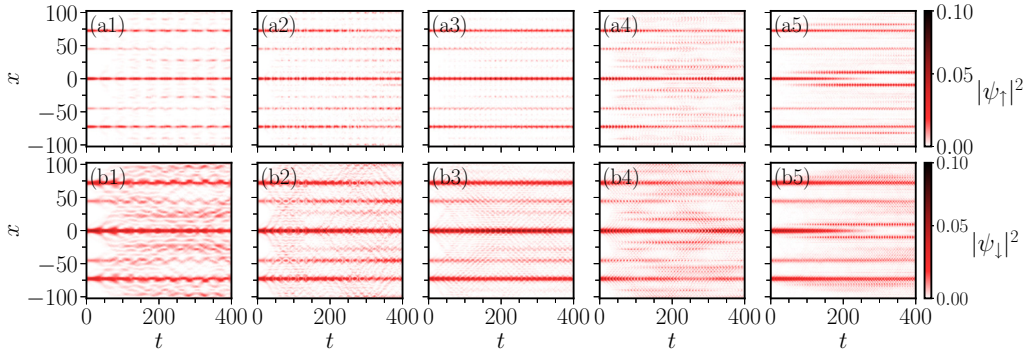


FIG. 9. Evolution of the density $|\psi_\uparrow|^2$ (top) and $|\psi_\downarrow|^2$ (bottom) with the self interaction $g = 0.3$ for different ω_{osc} as: (a1), (b1) $\omega_{osc} = 0.15$, (a2), (b2) $\omega_{osc} = 0.30$, (a3), (b3) $\omega_{osc} = 0.6$, (a4), (b4) $\omega_{osc} = 0.75$, and (a5), (b5) $\omega_{osc} = 0.9$. For different ω_{osc} different types of features are visible: at $\omega_{osc} = 0.15, 0.3$, each fragmented condensate starts expanding, but at $\omega_{osc} = 0.6$, fragmented parts do not show much expansion. In contrast, for other $\omega_{osc} = 0.75, 0.9$, more fragments are generated with time. The other parameters are $\Omega_0 = 0.3$, $\Omega_1 = 0.15$. Here (b1)–(b3) clearly show parquetlike patterns.

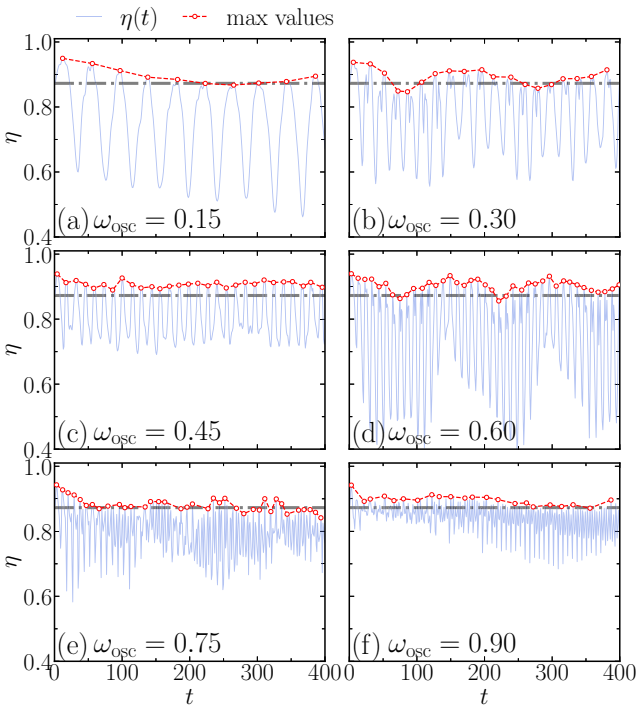


FIG. 10. Evolution of miscibility $\eta(t)$ for $g = 0.3$ and different oscillation frequencies as (a) $\omega_{\rm osc} = 0.1$, (b) $\omega_{\rm osc} = 0.2$, (c) $\omega_{\rm osc} = 0.4$, (d) $\omega_{\rm osc} = 0.6$, (e) $\omega_{\rm osc} = 0.8$, and (f) $\omega_{\rm osc} = 1.0$.. The black dash-dotted line indicates the initial miscibility $\eta(0) = 0.873$, obtained from the ground state before the time-dependent Rabi field is switched on ($\Omega_1 = 0$) The red circle dots show the evolution of the maximum values of $\eta(t)$.

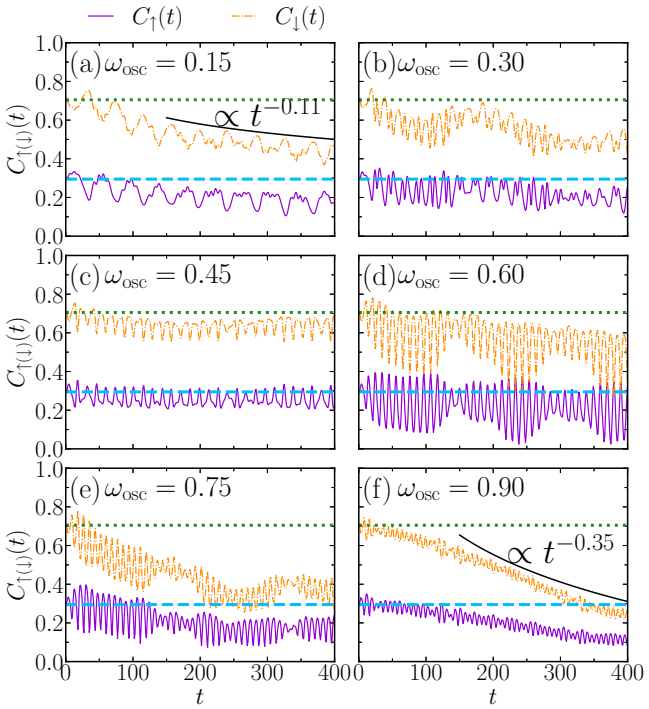


FIG. 11. Time evolution of the correlation function $C_{\uparrow(\downarrow)}(t)$ is shown at $g = 0.3$, $\Omega_0 = 0.3$, $\Omega_1 = 0.15$ for different oscillation frequencies $\omega_{\rm osc}$: (a) $\omega_{\rm osc} = 0.15$, (b) $\omega_{\rm osc} = 0.3$, (c) $\omega_{\rm osc} = 0.45$, (d) $\omega_{\rm osc} = 0.6$, (e) $\omega_{\rm osc} = 0.75$, and (f) $\omega_{\rm osc} = 0.9$. Here, the dashed line (sky blue color), and dotted line (green color) is drawn to compare with the static case $\omega_{\rm osc} = 0$. The expansion of the condensate can be characterized by highlighting the power-law decrement from $C_j(0)$.

values of $C_j(t)$ at $\omega_{\rm osc} = 0$ are indicated by a blue dashed line at $C_\uparrow \approx 0.3$ and a green dotted line at $C_\downarrow \approx 0.7$ in each panel. Notably, at $\omega_{\rm osc} = 0.15$ [Fig. 11(a)], the power-law decay of $C_j(t)$ reflects the expansion of the density from its initial distribution. The observed power-law behavior follows an exponent of $t^{-0.11}$. Similarly, for $\omega_{\rm osc} = 0.3$ [Fig. 11(b)], although $C_j(t)$ decreases, the absence of a power-law trend indicates the suppression of condensate expansion as we have seen in the noninteracting case (Fig. 8). Similarly, at $\omega_{\rm osc} = 0.45, 0.6$ [Figs. 11(c) and 11(d)], the decrement of $C_j(t)$ is further suppressed. On the other hand, for $\omega_{\rm osc} = 0.75, 0.9$, the relatively larger power-law decay rate demonstrates the expansion and possibly further fragmentation of the condensate.

As a result, we observe that the overall influence of the periodic Rabi frequency on the condensate is qualitatively similar to that in the noninteracting case. However, the interference of spin jets from different $\pm x_i$ minima makes the treelike expansion pattern in the noninteracting case similar to a much richer parquetlike pattern in the presence of interactions.

V. CONCLUSION AND FUTURE OUTLOOK

We have systematically investigated the localization and driven dynamics of a Rabi-coupled Bose-Einstein condensate subjected to a quasiperiodic potential in one spin component while the other one is potential free. By solving the Gross-Pitaevskii equation, we have explored how the Rabi coupling, the potential, and nonlinear interactions jointly influence the ground-state and the spatiotemporal characteristics of the condensate dynamics. For the linear condensates the results obtained by the imaginary time evolution align well with those obtained from the eigenmode analysis, highlighting the robustness of the induced localization mechanism.

In the absence of nonlinear interactions, we observe that the induced localization, where each component influences localization on the other, occurs when Rabi coupling exceeds a threshold value. With the introduction of self-interactions, both components exhibit localized and fragmented structures of the condensate.

After obtaining the ground state, we have studied the dynamics of the condensate under a periodically modulated Rabi frequency. When the driving frequency resonates with the intrinsic excitation modes of the localized system, we observe dynamically induced delocalization in both components accompanied by population redistribution. At higher harmonics of the resonant frequency, the condensate transitions into fragmented states, indicating mode-selective excitation. To quantitatively characterize these dynamical states, we have analyzed the evolution of miscibility and the temporal correlation functions of the spin components. Notably, similar features of drive-induced delocalization persist in the presence of interactions.

Here we propose a feasible experimental scheme to realize spin-dependent potentials in pseudospin-1/2 condensates. To generate such potentials, Bragg diffraction can be employed to selectively tune out specific wavelengths of optical lattices [60]. The experiment begins by creating a BEC trapped under a superimposed optical lattice potential $U_1(x)$ and $U_2(x)$. Initially, atoms are condensed in one of the hyperfine states, and a short laser pulse is applied, causing Bragg diffraction into higher momentum states. Subsequently, the lattice wavelengths are finely tuned so that atoms in the spin-up component experience only $U_1(x)$, while those in spin-down interact solely with $U_2(x)$. This approach has previously been used to realize binary BECs in spin-dependent twisted-bilayer lattices [60]. For our model, once the condensate is loaded into spin-dependent lattices, one of the lattice potential is slowly ramped down to avoid excitations, allowing that component to become free from trapping while the other is confined with the optical lattice. Finally, an external magnetic field that couples the components acts as the linear Rabi coupling for the GP model.

The induced localization and drive-induced delocalization explored in this work open up several promising directions for future research. One particularly intriguing avenue involves the competitive interplay between noncommuting spin-orbit and Rabi couplings on the condensate density components. Studying their combined effects within this hybrid setup could yield rich physics. Additionally, various sets of intra- and interspecies interactions may produce phases with separated components [27], thereby introducing new dynamical behaviors under time-modulated Rabi driving. In addition to these theoretical proposals, our findings help to engineer hybrid trapping of BECs in experiments where one component can be controlled by tuning the other component when they are coupled. Also, it can be of interest to design an experiment to probe a controlled induced localization-delocalization transition in ultracold atomic gases.

ACKNOWLEDGMENTS

S.K.S. would like to acknowledge the supercomputing facilities Param-Ishan and Param-Kamrupa at IITG, where all numerical simulations are performed. The work of E.Ya.S. is supported through Grants No. PGC2018-101355-B-I00 and No. PID2021-126273NB-I00 funded by MIUCI/AEI/10.13039/501100011033 and by the ERDF 'A way of making Europe', and by the Basque Government through Grant No. IT1470-22.

DATA AVAILABILITY

The data that support the findings of this article are not publicly available. The data are available from the authors upon reasonable request.

APPENDIX A: ANALYTICAL APPROACHES AND SCALING ANALYSIS

Here we consider analytical approaches to the induced by the Rabi-coupling localization for several realizations of interest. As in the main text, we assume self-interaction $g_{\uparrow\uparrow} = g_{\downarrow\downarrow} = g$ with no cross-spin coupling and present the GPEs as:

$$\mu\psi_\uparrow = \left[-\frac{1}{2}\frac{d^2}{dx^2} + g|\psi_\uparrow|^2 + V_\uparrow(x)\right]\psi_\uparrow + \Omega_0\psi_\downarrow, \quad \text{(A1a)}$$

$$\mu\psi_\downarrow = \left[-\frac{1}{2}\frac{d^2}{dx^2} + g|\psi_\downarrow|^2\right]\psi_\downarrow + \Omega_0\psi_\uparrow. \quad \text{(A1b)}$$

Below we consider a harmonic trap $V_\uparrow(x) = \lambda^2x^2/2 - V_0$, where V_0 is a uniform shift, which can influence the total wavefunction while acting on one spin component only. We present the wave function in the form with $\psi_\uparrow = \sqrt{N_\uparrow}\phi_\uparrow(x)$, $\psi_\downarrow = \sqrt{N_\downarrow}\phi_\downarrow(x)$, $\phi_\uparrow(x)$ and $\phi_\downarrow(x)$ are normalized to 1. Next, we consider how the spin-projected states behave in the case of strong $\Omega_0 > \lambda$ and weak $\Omega_0 \ll \lambda$ Rabi couplings. General results presented in Fig. 12 will be discussed below in terms of strong and weak couplings and briefly connected to the results for the quasiperiodic potential in the main text.

1. Strong Rabi coupling

We begin with the very strong Rabi coupling $\Omega_0 \gg \lambda$, where one expects $\langle\sigma_x\rangle = -1$ with $N_\uparrow = N_\downarrow = 1/2$ and $\phi_\downarrow(x) = -\phi_\uparrow(x)$. We introduce the ansatz $\phi^{[\mathrm{lim}]}(x) = \phi_\downarrow(x) = -\phi_\uparrow(x) = \exp(-x^2/2a^2)/\sqrt{a}\pi^{1/4}$ and minimize the total energy with respect to a to obtain the ground state. The spin-diagonal kinetic energy [see Eq. (12)] for the spin-down state described by $\phi^{[\mathrm{lim}]}(x)$ is $1/8a^2$ and the total [sum of the kinetic and potential energies given by Eq. (11)] for spin-up state is $1/4a^2 + \lambda^2a^2/8$. By minimizing their sum we obtain $a_0 = 2^{1/4}/\sqrt{\lambda}$ and, as a result, Eqs. (11) and (12) yield for this state $E_k = E_{\mathrm{pot}} = \lambda/4\sqrt{2}$.

Closely to this limit, we obtain corrections with respect to the small $\lambda/\Omega_0 \ll 1$, where $N_\downarrow \neq N_\uparrow$ with $\phi_\uparrow(x) = \exp(-x^2/2a_\uparrow^2)/\sqrt{a_\uparrow}\pi^{1/4}$ and $\phi_\downarrow(x) = \exp(-x^2/2a_\downarrow^2)/\sqrt{a_\downarrow}\pi^{1/4}$ with $a_\uparrow = a_0$. Thus, we obtain $N_\downarrow - N_\uparrow = \sqrt{2}\lambda/8\Omega_0$ and $(a_\downarrow - a_0)/a_0 = \lambda/2\sqrt{2}\Omega_0$, demonstrating that the corrections are linear in the small λ/Ω_0 ratio. This asymptotic behavior matches well Fig. 2 with $\omega_0 \approx 0.54$ [see Eq. (4)] taken as the λ.

Next, we briefly discuss the effect of self-repulsion g on the state corresponding to $\phi^{[\mathrm{lim}]}(x)$ [see Eq. (14)]. According to this equation, here the total spin-diagonal contribution to the energy acquires the term $E_{\mathrm{int}} = g\chi^{[\mathrm{lim}]}/4$, where $\chi^{[\mathrm{lim}]} = 1/\sqrt{2\pi}a_0$ is the corresponding IPR. Minimization of total energy yields an increase in the width $\delta a = g/16\sqrt{\pi}\lambda$ with a relatively small effect of the nonlinearity. It increases the width of the state and, therefore, increases the spin-diagonal energy difference, decreasing the effect of a strong Rabi coupling on the state disproportion.

2. Weak Rabi coupling

Here we consider a weak Rabi coupling $\lambda/\Omega_0 \ll 1$ with nonzero V_0. We begin with assuming the spin-down wave

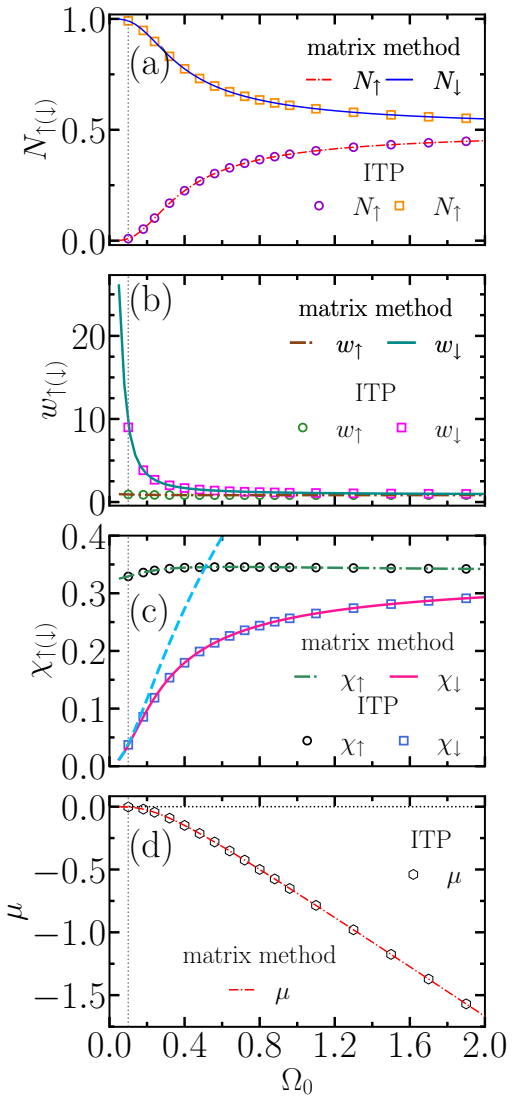


FIG. 12. (a) Variation of population as a function of Rabi coupling Ω_0 for $V = V_\uparrow(x) = x^2/2$. (b) Width $w_{\uparrow(\downarrow)}$, (c) IPR $\chi_{\uparrow(\downarrow)}$, and (d) the chemical potential as a function of Ω_0 at $g = 0$. The increasing IPR indicates that the condensate of spin-down component tends to localize due to the interaction with spin-up one. In (c), the dashed cyan line is drawn to show the comparison with $\chi_\downarrow = \sqrt{|\mu|/2}$ corresponding to $\psi_\downarrow$ in Eq. (A2).

function in the form

$$\psi_\downarrow = -2^{1/4}|\mu|^{1/4}\exp(-\sqrt{2|\mu|}|x|), \tag{A2}$$

normalized to $N_\downarrow = 1$ with the sufficient accuracy $\sim(\Omega_0/\lambda)^4$, and the corresponding $\chi_\downarrow = \sqrt{|\mu|/2}$. Then, the $\Omega_0\psi_\uparrow$ with $\psi_\uparrow = \sqrt{N_\uparrow}\phi_0(x)$, where $\phi_0(x) = \lambda^{1/4}\exp(-x^2\lambda/2)/\pi^{1/4}$ is the ground-state wave function in the $\lambda^2x^2/2$ potential is considered as the source of a weak perturbation potential localizing $\psi_\downarrow$ on the spatial scale $1/\sqrt{|\mu|} \gg 1/\sqrt{\lambda}$, with an example shown in Fig. 13. Thus, we can write Eq. (A1b) in the form:

$$\mu\psi_\downarrow = -\frac{1}{2}\frac{d^2}{dx^2}\psi_\downarrow + \frac{\Omega\sqrt{N_\uparrow}}{2^{1/4}|\mu|^{1/4}}\phi_0(x)\psi_\downarrow \tag{A3}$$

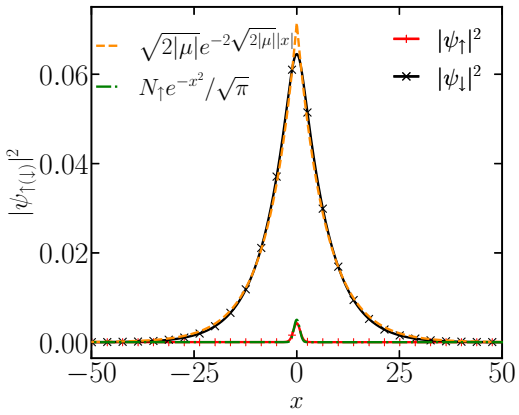


FIG. 13. The condensate density profile at $\Omega_0 = 0.1$ with the harmonic trap configuration as: $V_\uparrow(x) = x^2/2, V_\downarrow(x) = 0$. The numerical density profiles $|\psi_{\uparrow(\downarrow)}|^2$ are compared with analytical expressions for harmonic oscillator ($|\psi_\uparrow|^2$) and exponential localization ($|\psi_\downarrow|^2$).

and obtain for a weak narrow potential [61].

$$\mu = -\frac{1}{2\sqrt{2}}\frac{\Omega_0^2 N_\uparrow}{|\mu|^{1/2}}\left(\int_{-\infty}^{\infty}\phi_0(x)dx\right)^2, \tag{A4}$$

resulting in the relation between μ and $N_\uparrow$:

$$\mu = -\left(\sqrt{\frac{\pi}{2}}\frac{\Omega_0^2}{\lambda^{1/2}}N_\uparrow\right)^{2/3}. \tag{A5}$$

Next, to obtain second relation between μ and $N_\uparrow$, we use at $\sqrt{|\mu|}|x| \ll 1$, Eq. (A1a) with Eq. (A2) in the form:

$$\mu\sqrt{N_\uparrow}\phi_0(x) = \left(\frac{\lambda}{2} + V_0\right)\sqrt{N_\uparrow}\phi_0(x) - 2^{1/4}\Omega_0|\mu|^{1/4}. \tag{A6}$$

Multiplying both sides of Eq. (A6) by $\phi_0(x)$ and integrating we obtain after neglecting the left-hand side of this equation as the higher-order term in Ω_0:

$$N_\uparrow = 32\pi\frac{\Omega_0^4}{(\lambda + 2V_0)\lambda^3}; \quad \mu = -8\pi\frac{\Omega_0^4}{(\lambda + 2V_0)^{2/3}\lambda^{7/3}}. \tag{A7}$$

Notice that at $V_0 = 0$ we obtain a simple relation: $\mu = -\Omega_0 N_\downarrow/4$ in agreement with numerical calculations. The difference between spin-dependent localizations can be seen with the products $w_\uparrow\chi_\uparrow \approx 0.300 \approx 1/2\sqrt{\pi}$, as expected for the harmonic oscillator and $w_\downarrow\chi_\downarrow \approx 0.343 \approx 1/2\sqrt{2}$, corresponding to the exponential localization.

With the knowledge of the induced localization for harmonic oscillator, we can understand the behavior of the condensate in the quasiperiodic potential. At large and moderate Ω_0 it is very similar to the behavior in the harmonic oscillator potential with the frequency ω_0. With the decrease in Ω_0 the spin-down component spreads as $\chi_\downarrow^{-1} \sim 1/\sqrt{|\mu|} \sim \omega_0^{3/2}/\Omega_0^2$ and at $\Omega_0^{[cr]}$ corresponding to $\chi_\downarrow x_1 \lesssim 1$ extends to the wing minima causing the extension of the spin-up component followed by a fast increase in the width of both. Thus, from Eq. (4) we can see that at the rescaling of the quasiperiodic potential as $(\tilde{V}_1, \tilde{V}_2) = \nu(V_1, V_2)$ and $(\tilde{k}_1, \tilde{k}_2) = \kappa(k_1, k_2)$, the critical $\tilde{\Omega}_0^{[cr]}$ rescales as $\nu^{-3/8}\kappa^{-1/4}$. At a very small Ω_0

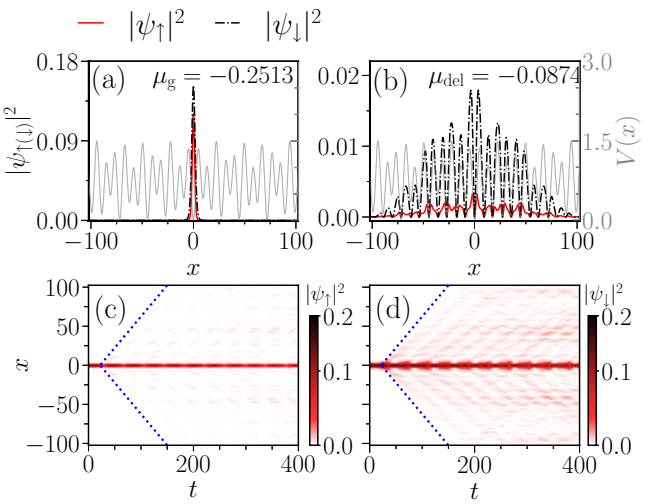


FIG. 14. (Top) The condensate density $|\psi_{\uparrow(\downarrow)}|^2$ associated with the ground state (a) and the excited state (b) of the coupled GPEs. (Bottom) Pseudo-color-map representation of the condensate densities (c) $|\psi_\uparrow|^2$ and (d) $|\psi_\downarrow|^2$ at $\Omega_0 = 0.4, \Omega_1 = 0.2, \omega_{\rm osc} = 0.1639$. Here, the oscillation frequency $\omega_{\rm osc} = 0.1639$ is obtained by taking the energy difference between the ground (a) and excited states (b) of the system as $\omega_{\rm osc} \approx |\mu_g - \mu_{\rm ex}| \approx 0.1639$. Other parameters are $V_2/V_1 = 0.5, V_1 = 1.0, g = 0$.

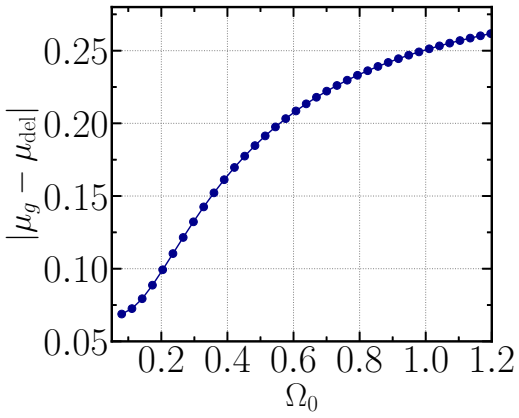


FIG. 15. Variation of the resonant frequency $\omega_{\rm osc}$ obtained by calculating the difference as $|\mu_g - \mu_{\rm del}|$ with Rabi coupling Ω_0 by keeping $V_2/V_1 = 0.5$, $V_1 = 1.0$, and $g = 0$. The resonant frequency initially increases almost linearly with Ω_0 and then saturates at higher values of Ω_0.

the width follows that for free particle localized in a one-dimensional box.

Now we discuss the role of the self-interaction in different spin components. Following Eq. (14), for this purpose we compare the quantities $N_\uparrow^2\chi_\uparrow \sim \Omega_0^8\lambda^{-15/2}$ and $\chi_\downarrow \sim \sqrt{|\mu|} \sim \Omega_0^2\lambda^{-3/2}$. Thus, in weak Rabi fields, self-interaction is much stronger in the spin-down component than in the spin-up one since the spin-up one has a low occupation probability. Thus, while the spin-up component interacts with the external potential, the spin-down component holds the self-interaction. A more detailed comparison of $g\chi_\downarrow$ and $|\mu|$ shows that self-interactions play an essential destructive role in the induced localization at $g \sim \sqrt{|\mu|} \sim 4\sqrt{\pi}\Omega_0^2\lambda^{-3/2}$, and this estimate is valid for other types of self-interaction with $g = g_{\uparrow\uparrow} = g_{\downarrow\downarrow} = g_{\uparrow\downarrow} = g_{\downarrow\uparrow}$ or $g = g_{\uparrow\downarrow} = g_{\downarrow\uparrow}, g_{\uparrow\uparrow} = g_{\downarrow\downarrow} = 0$.

APPENDIX B: RESONANT FREQUENCY FOR DELOCALIZATION

Here we discuss estimation of the resonant frequency for noninteracting BECs using the matrix method. The solution of coupled GPEs [(A1a) and (A1b)] computes eigenvalues associated with the ground and excited states of the Hamiltonian, where the lowest eigenvalue corresponds to the ground state [see Fig. 2(d)]. Here we utilize the difference between the ground-state and excited-state eigenvalues to obtain the approximate resonant frequency that drives the condensate delocalization.

We begin by solving the coupled GPE with quasiperiodic trap subjected to spin-up component by keeping $\Omega_0 = 0.4$. Subsequently, first 50 eigenvalues are obtained, in which the zeroth eigenvalue $\mu_g \equiv \mu^{[0]} = -0.2513$ represents the ground-state chemical potential [see Fig. 14(a)]. Following that, we examine excited states eigenvalues $(\mu_{\rm ex}^1, \mu_{\rm ex}^2, \mu_{\rm ex}^3 \ldots \mu_{\rm ex}^{50})$ and wave function in order to find the appropriate delocalized condensate. We found that for low-energy eigenstates, both components are localized symmetrically on either side of $x = 0$, occupying different minima of the potential. For higher excited states, where $|\mu|$ is close to zero, the eigenstates are extended all over the space, overcoming the effect of the potential. We have chosen those eigenstates as the delocalized states. For example, in Fig. 14(b), we present the condensate density with eigenvalue $\mu_{\rm del} = \mu_{\rm ex}^{23} = -0.0874$, where the density efficiently tunnels through the quasiperiodic trap. Therefore, the energy difference between the μ_g and $\mu_{\rm del}$ can be defined as the energy required to efficiently tunnel the condensate from the central minimum. Therefore, the approximate resonant frequency turns out to be $\omega_{\rm osc} \approx |\mu_g - \mu_{\rm del}| \approx 0.1639$ for $\Omega_0 = 0.4$.

Next, in Figs. 14(c) and 14(d), we show the evolution of condensate density $|\psi_\uparrow|^2$, and $|\psi_\downarrow|^2$, respectively, by keeping $\Omega_0 = 0.4, \Omega_1 = 0.2$, and oscillation frequency at $\omega_{\rm osc} = 0.1639$. Under this periodic driving, the condensate exhibits uniform expansion, albeit with a lower intensity compared to the case of $\omega_{\rm osc} = 0.2$ shown in Figs. 5(a2) and 5(b2). This suggests that $\omega_{\rm osc} \approx 0.1639$ resonantly drives the delocalization. It is important to note that, although the resonant frequency is estimated here by taking $\Omega_0 = 0.4$, the Ω_1 term in $\Omega(t)$ make the dynamics nonlinear and, thus, effectively modifies the resonant frequency for delocalization.

In Fig. 15, we illustrate the variation of the resonant frequency as a function of Ω_0. For low values of Ω_0, the resonant frequency increases almost linearly with Ω_0, followed by a saturation trend at larger values, where in the ground state the components behave as Gaussian localized states strongly localized in harmonic confinement with $N_\uparrow \approx N_\downarrow$. Under such conditions, the potential-free spin-down component closely follows the spin-up component. Although the matrix method gives only an approximate value of the resonant frequency, it provides valuable insights into the Rabi-driven delocalization of a condensate.

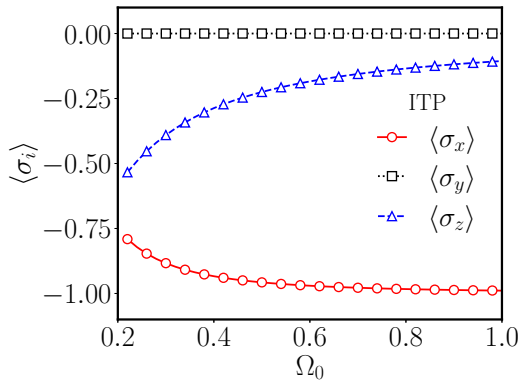


FIG. 16. Variation of $\langle\sigma_x\rangle$, $\langle\sigma_y\rangle$, and $\langle\sigma_z\rangle$ with Rabi coupling Ω_0. The variation of $\langle\sigma_x\rangle$, and $\langle\sigma_y\rangle$ demonstrates the change in the spin polarization with the variation of Ω_0. The other parameters are $V_2/V_1 = 0.5, V_1 = 1.0, g = 0$.

APPENDIX C: EFFECT OF RABI COUPLING ON SPIN POLARIZATION

Here we demonstrate the role of Rabi coupling in formation of spin polarization of the BEC. The spin polarization can be defined by attributing spin-dependent observables as:

$$\langle\sigma_x\rangle = \int_{-\infty}^{\infty} (\psi_\uparrow^\dagger \psi_\downarrow + \psi_\downarrow^\dagger \psi_\uparrow) dx, \tag{C1}$$

$$\langle\sigma_y\rangle = \mathrm{i}\int_{-\infty}^{\infty} (\psi_\uparrow^\dagger \psi_\downarrow - \psi_\downarrow^\dagger \psi_\uparrow) dx, \tag{C2}$$

$$\langle\sigma_z\rangle = \int_{-\infty}^{\infty} (|\psi_\uparrow|^2 - |\psi_\downarrow|^2) dx. \tag{C3}$$

Figure 16 shows the variation of the ground-state spin-related observables $\langle\sigma_i\rangle$ as a function of Ω_0. As expected, with the increase in Ω_0, $\langle\sigma_x\rangle$ tends to -1, and $\langle\sigma_z\rangle$ characterizing the spin polarization ($\langle\sigma_z\rangle = N_\uparrow - N_\downarrow$) of the system approaches zero as the spin components balance each other with population exchange. Such modifications of spin polarization are well known in multicomponent BECs with unequal self-interactions. Here, however, we demonstrate that within this spin-asymmetric potential model, the spin polarization $\langle\sigma_i\rangle$ components can be tuned effectively even in a linear condensate.

[1] P. W. Anderson, Absence of diffusion in certain random lattices, Phys. Rev. **109**, 1492 (1958).

[2] D. S. Wiersma, P. Bartolini, A. Lagendijk, and R. Righini, Localization of light in a disordered medium, Nature (London) **390**, 671 (1997).

[3] F. Scheffold, R. Lenke, R. Tweer, and G. Maret, Localization or classical diffusion of light? Nature (London) **398**, 206 (1999).

[4] T. Schwartz, G. Bartal, S. Fishman, and M. Segev, Transport and Anderson localization in disordered two-dimensional photonic lattices, Nature (London) **446**, 52 (2007).

[5] C. M. Aegerter, M. Störzer, S. Fiebig, W. Bührer, and G. Maret, Observation of Anderson localization of light in three dimensions, J. Opt. Soc. Am. A **24**, A23 (2007).

[6] J. Topolancik, B. Ilic, and F. Vollmer, Experimental observation of strong photon localization in disordered photonic crystal waveguides, Phys. Rev. Lett. **99**, 253901 (2007).

[7] R. Dalichaouch, J. P. Armstrong, S. Schultz, P. M. Platzman, and S. L. McCall, Microwave localization by two-dimensional random scattering, Nature (London) **354**, 53 (1991).

[8] C. Dembowski, H.-D. Gräf, R. Hofferbert, H. Rehfeld, A. Richter, and T. Weiland, Anderson localization in a string of microwave cavities, Phys. Rev. E **60**, 3942 (1999).

[9] A. A. Chabanov, M. Stoytchev, and A. Z. Genack, Statistical signatures of photon localization, Nature (London) **404**, 850 (2000).

[10] P. Pradhan and S. Sridhar, Correlations due to localization in quantum eigenfunctions of disordered microwave cavities, Phys. Rev. Lett. **85**, 2360 (2000).

[11] R. Weaver, Anderson localization of ultrasound, Wave Motion **12**, 129 (1990).

[12] J. Billy, V. Josse, Z. Zuo, A. Bernard, B. Hambrecht, P. Lugan, D. Clément, L. Sanchez-Palencia, P. Bouyer, and A. Aspect, Direct observation of Anderson localization of matter waves in a controlled disorder, Nature (London) **453**, 891 (2008).

[13] G. Roati, C. D'Errico, L. Fallani, M. Fattori, C. Fort, M. Zaccanti, G. Modugno, M. Modugno, and M. Inguscio, Anderson localization of a non-interacting Bose–Einstein condensate, Nature (London) **453**, 895 (2008).

[14] L. Sanchez-Palencia, Smoothing effect and delocalization of interacting Bose-Einstein condensates in random potentials, Phys. Rev. A **74**, 053625 (2006).

[15] L. Sanchez-Palencia, D. Clément, P. Lugan, P. Bouyer, G. V. Shlyapnikov, and A. Aspect, Anderson localization of expanding Bose-Einstein condensates in random potentials, Phys. Rev. Lett. **98**, 210401 (2007).

[16] S. K. Adhikari and L. Salasnich, Localization of a Bose-Einstein condensate in a bichromatic optical lattice, Phys. Rev. A **80**, 023606 (2009).

[17] Y. Cheng and S. K. Adhikari, Matter-wave localization in a random potential, Phys. Rev. A **82**, 013631 (2010).

[18] Y. Cheng and S. K. Adhikari, Localization of collisionally inhomogeneous condensates in a bichromatic optical lattice, Phys. Rev. A **83**, 023620 (2011).

[19] L. W. Cheuk, A. T. Sommer, Z. Hadzibabic, T. Yefsah, W. S. Bakr, and M. W. Zwierlein, Spin-injection spectroscopy of a spin-orbit coupled Fermi gas, Phys. Rev. Lett. **109**, 095302 (2012).

[20] M. Zohra and A. Boudjemâa, Anderson localization of elementary excitations in disordered binary Bose mixtures: Effects of the Lee-Huang-Yang quantum and thermal corrections, Phys. Rev. A **110**, 053305 (2024).

[21] Y.-J. Lin, K. Jiménez-García, and I. B. Spielman, Spin-orbit-coupled Bose-Einstein condensates, Nature (London) **471**, 83 (2011).

[22] Y. Cheng, G. Tang, and S. K. Adhikari, Localization of a spin-orbit-coupled Bose-Einstein condensate in a bichromatic optical lattice, Phys. Rev. A **89**, 063602 (2014).
[23] C. Li, F. Ye, Y. V. Kartashov, V. V. Konotop, and X. Chen, Localization-delocalization transition in spin-orbit-coupled Bose-Einstein condensate, Sci. Rep. **6**, 31700 (2016).
[24] S. K. Sarkar, R. Ravisankar, T. Mishra, P. Muruganandam, and P. Mishra, Signature of localization–delocalization in collisional inhomogeneous spin-orbit coupled condensates, J. Phys. B: At. Mol. Opt. Phys. **58**, 065001 (2025).
[25] K.-T. Xi, J. Li, and D.-N. Shi, Localization of a two-component Bose-Einstein condensate in a one-dimensional random potential, Phys. B: Condens. Matter **459**, 6 (2015).
[26] H. Zhang, S. Liu, and Y. Zhang, Anderson localization of a spin–orbit coupled Bose-Einstein condensate in disorder potential, Chin. Phys. B **31**, 070305 (2022).
[27] S. K. Sarkar, S. Mardonov, E. Ya Sherman, P. Muruganandam, and P. K. Mishra, Spin-dependent localization of spin–orbit and Rabi-coupled Bose-Einstein condensates in a random potential, New J. Phys. **27**, 023018 (2025).
[28] S. Mardonov, M. Modugno, and E. Y. Sherman, Dynamics of spin-orbit coupled Bose-Einstein condensates in a random potential, Phys. Rev. Lett. **115**, 180402 (2015).
[29] S. Mardonov, V. V. Konotop, B. A. Malomed, M. Modugno, and E. Y. Sherman, Spin-orbit-coupled soliton in a random potential, Phys. Rev. A **98**, 023604 (2018).
[30] Z. Gui, Z. Zhang, J. Su, H. Lyu, and Y. Zhang, Spin-orbit-coupling-induced phase separation in trapped Bose gases, Phys. Rev. A **108**, 043311 (2023).
[31] S. V. Manakov, On the theory of two-dimensional stationary self-focusing of electromagnetic waves, Sov. Phys. JETP **65**, 248 (1974).
[32] Y. Cheng and S. K. Adhikari, Spatially-antisymmetric localization of matter wave in a bichromatic optical lattice, Laser Phys. Lett. **7**, 824 (2010).
[33] W.-Y. Wang, F.-Q. Dou, and W.-S. Duan, Interaction induced localization of a spin–orbit-coupled Bose-Einstein condensate in a double-well potential, Eur. Phys. J. D **73**, 19 (2019).
[34] M. C. P. dos Santos and W. B. Cardoso, Anderson localization induced by interaction in linearly coupled binary Bose-Einstein condensates, Phys. Rev. E **103**, 052210 (2021).
[35] Y. Zhang, G. Chen, and C. Zhang, Tunable spin-orbit coupling and quantum phase transition in a trapped Bose-Einstein condensate, Sci. Rep. **3**, 1937 (2013).
[36] K. Jiménez-García, L. J. LeBlanc, R. A. Williams, M. C. Beeler, C. Qu, M. Gong, C. Zhang, and I. B. Spielman, Tunable spin-orbit coupling via strong driving in ultracold-atom systems, Phys. Rev. Lett. **114**, 125301 (2015).
[37] J. Struck, C. Ölschläger, R. L. Targat, P. Soltan-Panahi, A. Eckardt, M. Lewenstein, P. Windpassinger, and K. Sengstock, Quantum simulation of frustrated classical magnetism in triangular optical lattices, Science **333**, 996 (2011).
[38] F. Meinert, M. J. Mark, K. Lauber, A. J. Daley, and H.-C. Nägerl, Floquet engineering of correlated tunneling in the Bose-Hubbard model with ultracold atoms, Phys. Rev. Lett. **116**, 205301 (2016).
[39] F. K. Abdullaev, P. G. Kevrekidis, and M. Salerno, Compactons in nonlinear Schrödinger lattices with strong nonlinearity management, Phys. Rev. Lett. **105**, 113901 (2010).
[40] A. J. Olson, S.-J. Wang, R. J. Niffenegger, C.-H. Li, C. H. Greene, and Y. P. Chen, Tunable Landau-Zener transitions in a spin-orbit-coupled Bose-Einstein condensate, Phys. Rev. A **90**, 013616 (2014).
[41] J. M. Gomez Llorente and J. Plata, Modulation of spin–orbit coupled Bose–Einstein condensates: Analytical characterization of acceleration-induced transitions between energy bands, J. Phys. B: At. Mol. Opt. Phys. **57**, 235301 (2024).
[42] B. Deconinck, P. G. Kevrekidis, H. E. Nistazakis, and D. J. Frantzeskakis, Linearly coupled Bose-Einstein condensates: From Rabi oscillations and quasiperiodic solutions to oscillating domain walls and spiral waves, Phys. Rev. A **70**, 063605 (2004).
[43] H. E. Nistazakis, Z. Rapti, D. J. Frantzeskakis, P. G. Kevrekidis, P. Sodano, and A. Trombettoni, Rabi switch of condensate wave functions in a multicomponent Bose gas, Phys. Rev. A **78**, 023635 (2008).
[44] F. K. Abdullaev, M. Brtka, A. Gammal, and L. Tomio, Solitons and Josephson-type oscillations in Bose-Einstein condensates with spin-orbit coupling and time-varying Raman frequency, Phys. Rev. A **97**, 053611 (2018).
[45] A. Trombettoni, H. Nistazakis, Z. Rapti, D. Frantzeskakis, and P. Kevrekidis, Soliton dynamics in linearly coupled discrete nonlinear Schrödinger equations, Math. Comput. Simulat. **80**, 814 (2009).
[46] C.-F. Liu, M. Lu, and W.-Q. Liu, Dynamics of vector dark soliton induced by the Rabi coupling in one-dimensional trapped Bose–Einstein condensates, Phys. Lett. A **376**, 188 (2012).
[47] I. M. Merhasin, B. A. Malomed, and R. Driben, Transition to miscibility in a binary Bose–Einstein condensate induced by linear coupling, J. Phys. B: At. Mol. Opt. Phys. **38**, 877 (2005).
[48] I. M. Merhasin, B. A. Malomed, and R. Driben, Miscibility transition in a binary Bose-Einstein condensate induced by linear interconversion, Phys. Scr. **2005**, 18 (2005).
[49] G. Gligorić, A. Maluckov, M. Stepić, L. Hadžievski, and B. A. Malomed, Transition to miscibility in linearly coupled binary dipolar Bose-Einstein condensates, Phys. Rev. A **82**, 033624 (2010).
[50] E. Chiquillo, Quasi-one-dimensional spin-orbit- and Rabi-coupled bright dipolar Bose-Einstein-condensate solitons, Phys. Rev. A **97**, 013614 (2018).
[51] T. Kanna, A. Annamalar Sheela, and R. Babu Mareeswaran, Spatially modulated two- and three-component Rabi-coupled Gross–Pitaevskii systems, J. Phys. A: Math. Theor. **52**, 375201 (2019).
[52] H. Susanto, P. Kevrekidis, B. Malomed, and F. Abdullaev, Effects of time-periodic linear coupling on two-component Bose–Einstein condensates in two dimensions, Phys. Lett. A **372**, 1631 (2008).
[53] J.-C. Zhao, C.-D. Li, Y.-Q. Li, and J.-G. Wang, Rabi-coupled binary Bose-Einstein condensates with spatially modulated nonlinear spin-orbit coupling, Int. J. Theor. Phys. **60**, 3609 (2021).
[54] R. Ravisankar, D. Vudragović, P. Muruganandam, A. Balaž, and S. K. Adhikari, Spin-1 spin–orbit- and Rabi-coupled Bose–Einstein condensate solver, Comput. Phys. Commun. **259**, 107657 (2021).
[55] S. K. Sarkar, T. Mishra, P. Muruganandam, and P. K. Mishra, Quench-induced chaotic dynamics of Anderson-localized

interacting Bose-Einstein condensates in one dimension, Phys. Rev. A **107**, 053320 (2023).

[56] S. S. Rawat, S. K. Jha, M. K. Verma, and P. K. Mishra, quTARANG: A high-performance computing python package to study turbulence using the Gross-Pitaevskii equation, Comput. Phys. Commun. **315**, 109725 (2025).

[57] K. Nakamura, A. Kohi, H. Yamasaki, V. M. Pérez-García, and V. V. Konotop, Levitation of spinor Bose-Einstein condensates: Macroscopic manifestation of the Franck-Condon effect, Europhys. Lett. **80**, 50005 (2007).

[58] I. Březinová, L. A. Collins, K. Ludwig, B. I. Schneider, and J. Burgdörfer, Wave chaos in the nonequilibrium dynamics of the Gross-Pitaevskii equation, Phys. Rev. A **83**, 043611 (2011).

[59] E. V. Doggen and J. J. Kinnunen, Quench-induced delocalization, New J. Phys. **16**, 113051 (2014).

[60] Z. Meng, L. Wang, W. Han, F. Liu, K. Wen, C. Gao, P. Wang, C. Chin, and J. Zhang, Atomic Bose–Einstein condensate in twisted-bilayer optical lattices, Nature (London) **615**, 231 (2023).

[61] L. D. Landau and E. M. Lifshits, *Quantum Mechanics - Nonrelativistic Theory* (Elsevier, Amsterdam, 2013).